Supporting Information

Byrne et al. 10.1073/pnas.1001290107

SI Results

Optimization of Magnetite Formation in RS-1. Because of RS-1's reportedly weak magnetotactic behavior, this study initially focused on optimizing the growth of RS-1 to increase the magnetic properties of the cells. The strain from the German Collection of Microorganisms and Cell Cultures (DSMZ), grown in a standard medium, displayed a low level of magnetism as quantified by its low Cmag values of 1.02 to 1.05. RS-1 grown in a standard medium containing sulfate produces H_2S, which causes extracellular iron salts to precipitate as iron sulfide (1, 2). Under these conditions, the available pool of iron is lower and RS-1 produces fewer magnetite crystals. Therefore, the medium was modified to remove all sulfate, and pyruvate and fumarate were used as the electron donor and acceptor, respectively. The doubling time of RS-1 cultures grown under these conditions was between 10 and 11 h, which is similar to the doubling time in sulfate-reducing conditions (2). Cultures were also started from single colonies to reduce genetic variation. In addition, several types of chelated iron, including ferric EDTA, ferric quinate and ferric malate, and iron concentrations were tested with 100 to 200 μM ferric malate yielding cultures with Cmag ratios of 1.40 to 1.60. As a result of these optimization experiments, 100% of the cells contained magnetite crystals, which is in contrast to previous studies that have reported that anywhere from 30 to greater than 50% of cells do not contain crystals (2, 3). On average, each cell contained 12 to 15 crystals measuring an average of 60 nm in length, which is twice the previously reported number of crystals per cell and a 50% increase over the previously reported crystal length (2, 3) (Fig. S1).

Transient Growth in Iron Is Not Sufficient for Magnetite Formation. To investigate the possibility that the granules transform into magnetite, it was first determined if the amount of iron present in the granules was sufficient for magnetite formation. Iron-starved RS-1 cells were grown in medium with iron for 3 h, at which point the cells contained a maximal number of iron-phosphorus (Fe-P) granules but no magnetite crystals (Fig. S2). The cells were then washed and transferred to iron-free medium. If the Fe-P granules were precursors to magnetite, the magnetite crystals would form in the absence of additional, extracellular iron. However, the cells never became magnetic (Cmag = 1), although control cells transferred to medium containing iron did form magnetite [Cmag = 1.25; crystals verified by transmission electron microscopy (TEM)]. Although these results suggest that the Fe-P granules are not precursors to magnetite, they did not exclude the possibility that the Fe-P granules only develop into magnetite in the presence of a certain threshold of extracellular iron. To explore that possibility, we performed the pulse-chase NanoSIMS experiment detailed in the main text.

SI Materials and Methods

Growth Conditions and Medium Composition. *Desulfovibrio magneticus* sp. RS-1 was obtained from the DSMZ (DSM no. 13731) and grown in a modified version of the DSMZ's "*Desulfovibrio magneticus* medium," here called RS-1 growth medium (RGM). This medium contains 6 mM potassium monophosphate, 5 mM ammonium chloride, 10 mM fumaric acid disodium, 10 mM sodium pyruvate, and 4 mL per liter of modified Wolfe's mineral solution (prepared with no sulfate or iron) (1). The medium was adjusted to pH 7.3, aliquoted into sealed Balch tubes (10 mL) or bottles (100 mL), autoclaved, and bubbled with nitrogen gas. Before inoculating with cells, Wolfe's vitamins (0.8% total volume), 20 mM ferric malate (100 μM final), and 28.5 mM cysteine-HCl (285 μM final) were added, and the medium was bubbled with nitrogen gas again. Plates were made with RGM supplemented with 60 to 200 μM H_2SO_4, and agar was added to 1% (wt/vol). After autoclaving, vitamins, ferric malate (20 μM final concentration), and cysteine (285 μM final) were added. Plates were incubated in anaerobic jars (Oxoid). Both plates and liquid cultures were incubated at 30 °C. For experiments in which RS-1 was grown in the absence of iron, ferric malate was excluded from the medium and the glassware was soaked in oxalic acid solution for 24 h before use and then rinsed three times with distilled, de-ionized water. Cultures grown with and without iron had similar doubling times (10–11 h).

Cmag Readings. A light scattering assay was used to obtain Cmag ratios for the RS-1 cultures, as previously described (4).

Iron-Uptake Experiments. One-hundred-milliliter cultures of RS-1 were inoculated at a low cell number into medium containing no added iron and then allowed to grow for at least 2 d until they reached early log phase (OD_{400} of 0.03–0.05). Cmag readings were taken to confirm that the cells were nonmagnetic (Cmag = 1.00). Ferric malate was then added to a final concentration of 100 μM. At various times, cells were collected and prepared for transmission electron microscopy (TEM), cryo-ultramicrotomy, electron cryo-tomography, or Cmag readings. For the iron-uptake experiment analyzed by NanoSIMS, cells were grown for 3 h in RGM with 100 μM ferric malate containing naturally occurring iron (~92% ^{56}Fe). Then, the cells were filtered using a 0.22-μm filter and washed with RGM containing 100 μM ferric malate made with ^{57}Fe (94%, Cambridge Isotope Laboratories, Inc.) before being transferred to RGM with 100 μM ferric (^{57}Fe) malate in anaerobic bottles. To make the ferric (^{57}Fe) malate, iron-57 metal was dissolved in 5 M HCl for 3 d. When the iron was dissolved, the concentration was assessed by ferrozine assay (5), then adjusted to 250 mM ^{57}Fe in 2.6 M HCl, which was used to make a stock solution of 25 mM ferric (^{57}Fe) malate with 6 mM potassium phosphate, pH 7.4.

Whole-Cell TEM. Cells were placed on copper grids coated with 0.5% formvar in ethylene dichloride and incubated for 5 min, after which the grids were washed three times in distilled, de-ionized water and dried. No stain was used. The microscopy was performed using a transmission electron microscope (FEI Tecnai 12) operating at 100 kV equipped with a Gatan UltraScan 1000 (2 k × 2 k) camera.

TEM Analysis of Ultrathin Sections. The morphological characteristics and chemical composition of magnetite and other Fe-containing solid inclusions within the bacteria were investigated with TEM. Culture medium containing bacterial cells was fixed with 2.5% glutaraldehyde in 0.1 M sodium cacodylate buffer. The specimens were centrifuged for 2 min at 15,000 × *g* to form a pellet. After washing with buffer and a solution of 100% ethyl alcohol-H_2O, samples were dehydrated with 100% ethyl alcohol, and the pellet was embedded in low viscosity, thermally curing Epon resin. Ultrathin sections (70–100 nm) were cut from the resin blocks by using a Reichert-Jung Ultracut E ultramicrotome with a Diatome diamond knife. The sections were transferred onto 200-mesh Cu TEM grids with formvar support film for image analysis in a FEI Tecnai 12 equipped with a Gatan Bioscan CCD camera Model 792 and at an accelerating voltage of 120 kV in bright-field mode. To enhance the contrast in the

bacterial cells in the TEM images, selected samples were stained with lead citrate and uranium acetate. To image the true size and shape of the magnetite crystals, images were obtained using a variety of tilt angles. Lattice fringe images of the magnetite crystals were obtained from nonstained sections using a FEI Tecnai G^2 F20 cryo-STEM equipped with a Gatan Ultrascan 4000 4 k × 4 k CCD camera Model 895 at an accelerating voltage of 200 kV. Chemical composition was determined by energy dispersive spectroscopy using the EDAX Genesis microanalytical system.

Cryo-Ultramicrotomy and Cryo-Electron Tomography. Cells were collected by centrifugation at 8,000 × *g* for 10 min or filtering, washed twice in 1 mL of 1 mM PBS, layered with 1 mL 2.5% glutaraldehyde in PBS, and stored at 4 °C. Cryo-fixation and cryo-ultramicrotomy were performed as previously described (4). The ultrathin cryo-sections were imaged with the FEI Tecnai 12 TEM equipped with a Gatan Bioscan 792 1 k × 1 k CCD camera at an accelerating voltage of 120 kV in bright-field mode. For tomography and 3D reconstruction, a tilt series of images was recorded at room temperature using FEI tomography acquisition software from −70° to 70° every 2° using the FEI Tecnai G^2 F20 cryo-STEM equipped with a Gatan Ultrascan 4000 4 k × 4 k CCD camera model 895 at an accelerating voltage of 200 kV and nominal magnification of 19,000× and at a defocus of ∼2 μm. Images were binned by a factor of two, giving a pixel size of 1.16 nm at the specimen level. Images from −56° to 60° were used to calculate the tomogram (as higher tilt images were too dark) using the eTomo suite of programs (http://bio3d.colorado.edu) (6). Visualization and segmentation of the tomogram was done with IMOD and Amira (Visual Imaging).

NanoSIMS. Secondary ion mass spectroscopy (SIMS) imaging was performed using a NanoSIMS-50 Ion Microprobe (CAMECA) operating in scanning mode (7). The elemental mapping was performed on the same thin section previously observed by TEM. This combination provides complementary chemical information by SIMS in addition to the high spatial resolution structural information by TEM (8). The instrument is equipped with a magnetic spectrometer using a parallel detection system that could acquire simultaneously up to five chemical species. The two iron isotopes (^{56}Fe and ^{57}Fe) were detected as $^{56}Fe^{16}O^-$ and $^{57}Fe^{16}O^-$ ions. However, a limitation with spacing between adjacent detectors does not permit simultaneous detection of these two ion species. Therefore, two sequential acquisitions were necessary. Besides FeO^- ions, a $^{12}C^{14}N^-$ map was acquired to visualize the cell layout. $^{31}P^-$ distribution was mapped to investigate a possible colocation of Fe and P in some cellular inclusions. The primary ion beam is generated from a caesium source. The primary ion intensity was around 1 pA during experiments, with a probe size down to 100 nm in diameter (defined as 16–84% rise distance of the signal intensity). The probe was stepped over the sample in a 256 × 256 pixel raster of 10 to 15 μm to generate secondary ion images. The typical dwell time was 60 ms per pixel for each acquisition set ($^{12}C^{14}N^-$, $^{31}P^-$ and $^{56}Fe^{16}O^-$ then $^{12}C^{14}N^-$, $^{31}P^-$ and $^{57}Fe^{16}O^-$). To ensure proper colocalization of the observed structures for all of the ion species between the two acquisition sets, image processing was performed using ImageJ (http://rsb.info.nih.gov/ij/). Furthermore, these processed elemental maps were cross correlated with TEM images, using ImageJ software with the TurboReg plugin (http://bigwww.epfl.ch/thevenaz/turboreg).

Cryo-Electron Tomography of Fully Hydrated, Unstained Cells. Cells were collected by centrifugation at 8,000 × *g* for 10 min and then resuspended in a 1:100 volume of 50 mM Tris, pH 9.0 and 10 mM EDTA. The cells were flash-frozen in liquid nitrogen and thawed with no agitation. The freeze-thaw was repeated four to five times and the cells were stored at −80 °C. Two-hundred mesh lacey carbon grids (Ted Pella 01881-F) were used for all cryo-electron microscopy. Grids were pretreated by glow-discharge for 20 seconds. Next, 4 μL of a 1:4 mix of 10-nm nano gold (Ted Pella 15703–20) and de-ionized H_2O was added to the grid for 5 min, then blotted on Whatman #1 filter paper. RS-1 cells were mixed 4:1 with 10 nm nano gold. Next, 3 μL of the mix was applied to the glow-discharged grids and blotted for 3 s in 90 to 100% humidity using a Vitrobot Mark IV (FEI). Samples were held in the humidity chamber of the Vitrobot after blotting for a drain time of 0.5 s. The grids were then plunged into liquid ethane and then transferred into liquid nitrogen for storage. All images were acquired on a JOEL-3100 series electron microscope equipped with a field emission gun operating at 300 kV, a Gatan 795 2 k × 2 k CCD camera, an Omega energy filter, and a cryo-transfer stage cooled with liquid nitrogen to 80 K. All tomographic tilt series were recorded under low-dose conditions. Typical angular ranges for single tilt data sets were between +65° and −65°, ± 5° with increments of 1°. All tomography data sets were recorded semiautomatically using SerialEM adapted for JEOL microscopes (http://bio3d.colorado.edu/). Images were recorded using nominal microscope magnifications of 25 k× or 20 k×, giving a pixel size at the CCD of 1 or 1.2 nm, respectively. Under-focus values ranged between 10 ± 0.5 and 12 ± 0.5 μm, with an energy filter width of 30 or 35 eV. For all data sets, the maximum dose used per complete tilt series or dual axis tilt series was 150 $e^-/Å^2$, with typical values of ≈100 to 130 $e^-/Å^2$. Raw tomographic image stacks were aligned either manually with the eTomo suite of programs (http://bio3d.colorado.edu/) or automatically using the software RAPTOR (9). Tomographic reconstructions were constructed using the eTomo suite of programs and tomograms were viewed using IMOD (6).

1. Sakaguchi T, Burgess JG, Matsunaga T (1993) Magnetite formation by a sulfate-reducing bacterium. *Nature* 365:47–49.
2. Sakaguchi T, Arakaki A, Matsunaga T (2002) *Desulfovibrio magneticus* sp. nov., a novel sulfate-reducing bacterium that produces intracellular single-domain-sized magnetite particles. *Int J Syst Evol Microbiol* 52:215–221.
3. Posfai M, et al. (2006) Properties of intracellular magnetite crystals produced by Desulfovibrio magneticus strain RS-1. *Earth Planet Sci Lett* 249:444–455.
4. Komeili A, Vali H, Beveridge TJ, Newman DK (2004) Magnetosome vesicles are present before magnetite formation, and MamA is required for their activation. *Proc Natl Acad Sci USA* 101:3839–3844.
5. Stookey LL (1970) Ferrozine—A new spectrophotometric reagent for iron. *Anal Chem* 42:779–781.
6. Mastronarde DN (1997) Dual-axis tomography: An approach with alignment methods that preserve resolution. *J Struct Biol* 120:343–352.
7. Guerquin-Kern JL, Wu TD, Quintana C, Croisy A (2005) Progress in analytical imaging of the cell by dynamic secondary ion mass spectrometry (SIMS microscopy). *Biochim Biophys Acta* 1724:228–238.
8. Azari F, et al. (2008) Intracellular precipitation of hydroxyapatite mineral and implications for pathologic calcification. *J Struct Biol* 162:468–479.
9. Amat F, et al. (2008) Markov random field based automatic image alignment for electron tomography. *J Struct Biol* 161:260–275.

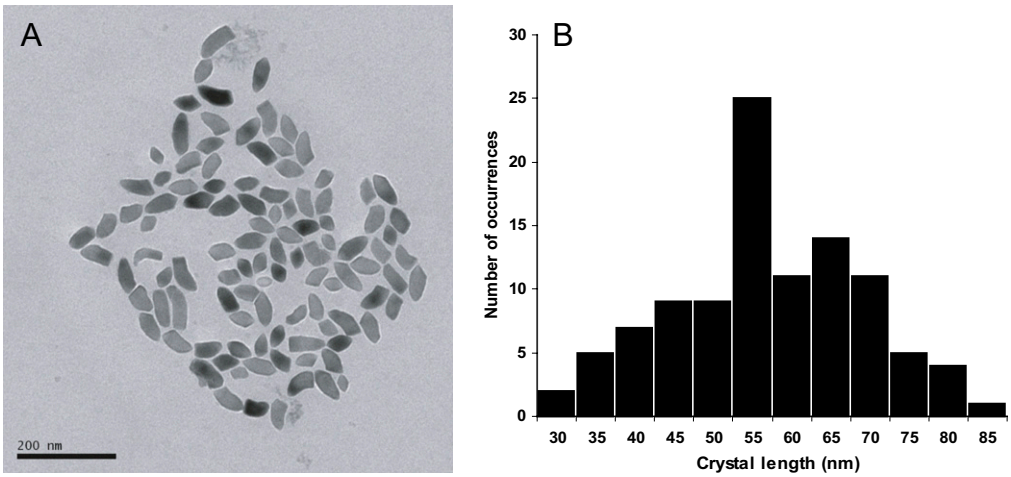

Fig. S1. The magnetite crystals from RS-1 are bullet-shaped and range in length from 32 to 85 nm. (*A*) A transmission electron micrograph of magnetite crystals isolated from lysed RS-1 cells. (*B*) A histogram of crystal lengths from *A*.

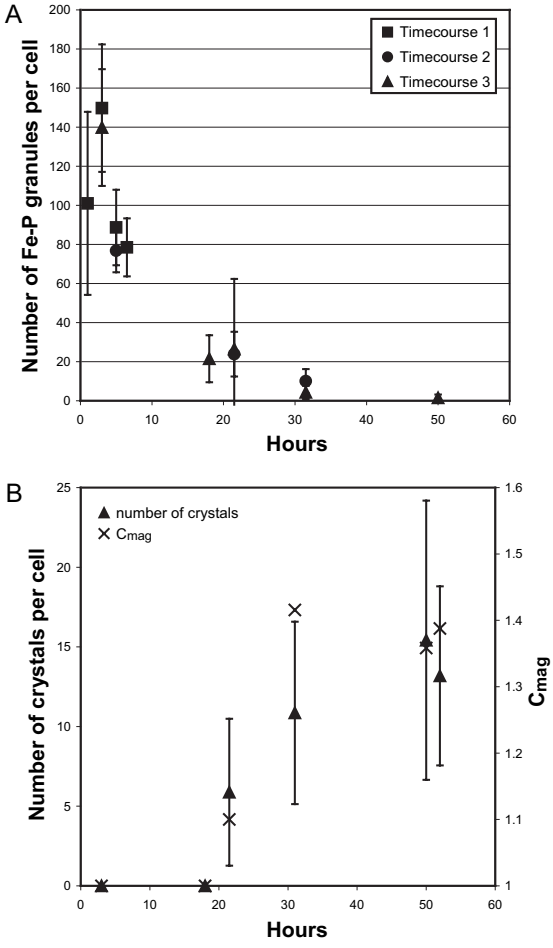

Fig. S2. After supplying iron to iron-starved RS-1 cells, the number of Fe-P granules increases initially then decreases. Magnetite crystals first appear around 21 h after iron addition and the number per cell increases with time. (*A*) The average number of Fe-P granules per cell over time from three independent time courses. (*B*) The average number of magnetite crystals per cell over time in one representative time course and the corresponding Cmag ratios for the cultures. Error bars in *A* and *B* indicate SD of the average number of granules and crystals per cell, respectively, as seen by TEM of whole cells.

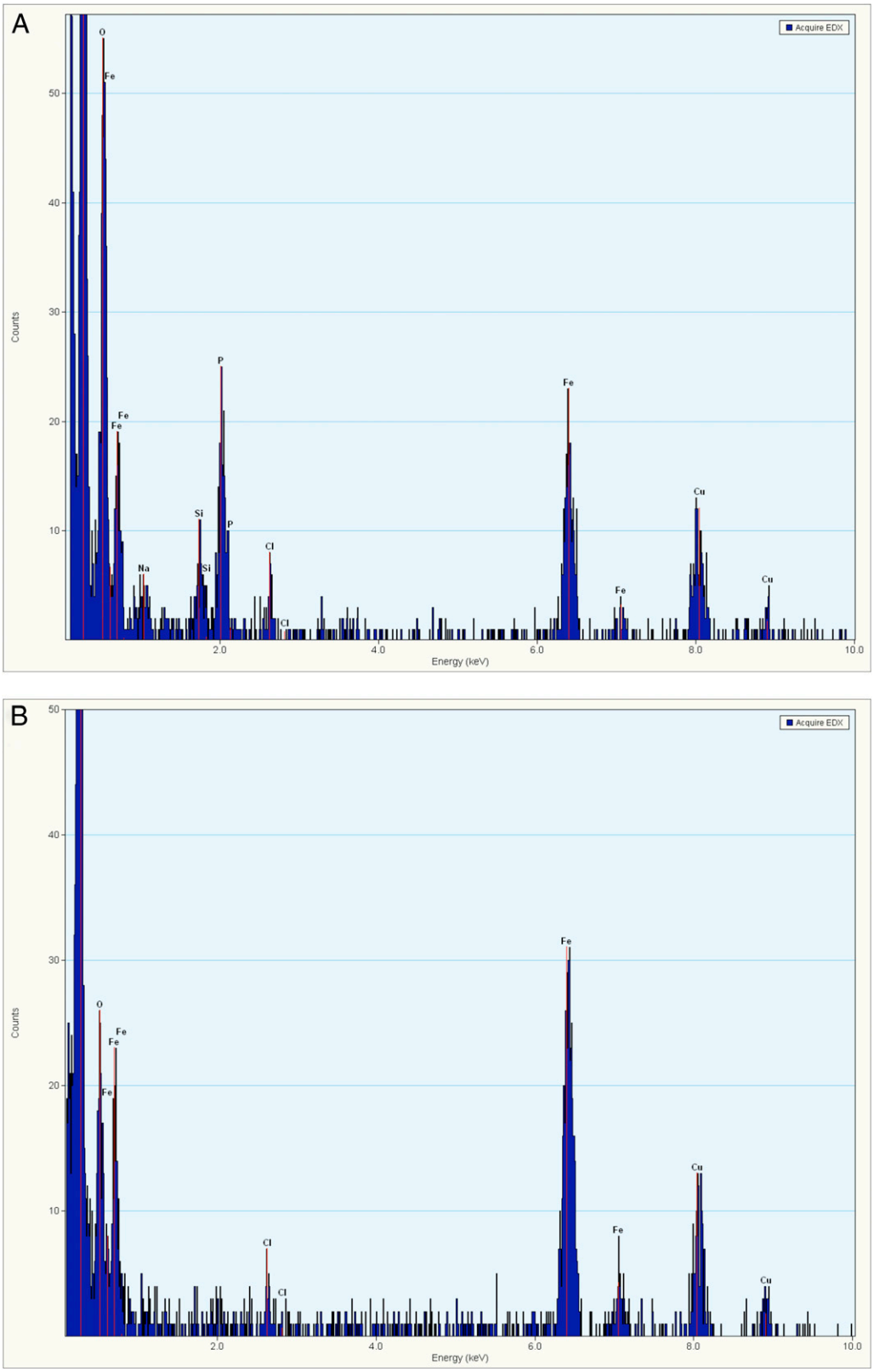

Fig. S3. Energy-dispersive X-ray spectroscopy analysis of the granules in 3 h post iron-addition samples (*A*) and magnetite crystals (*B*) at the 96-h time point shows that the granules contain iron, phosphorus, and oxygen, although the magnetite crystals contain iron and oxygen. As can be seen, the iron signal is comparable for the two types of particles, indicating significant amounts of iron are present in the Fe-P granules. The copper signal comes from the copper grids, and the carbon signal (the large peak at the low keV portion of the graph) comes from both the cell background and the carbon coating on the grids.

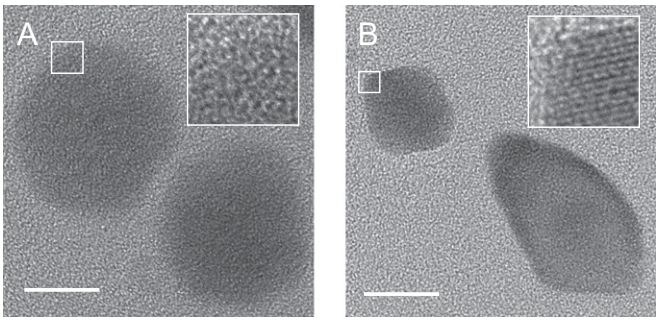

Fig. S4. High-resolution TEM (HRTEM) shows that the granules are amorphous but the magnetite exhibits a crystalline lattice. (*A*) HRTEM of an iron-phosphorus granule. (Scale bar = 20 nm.) (*B*) HRTEM of a magnetite crystal. (Scale bar = 20 nm.)

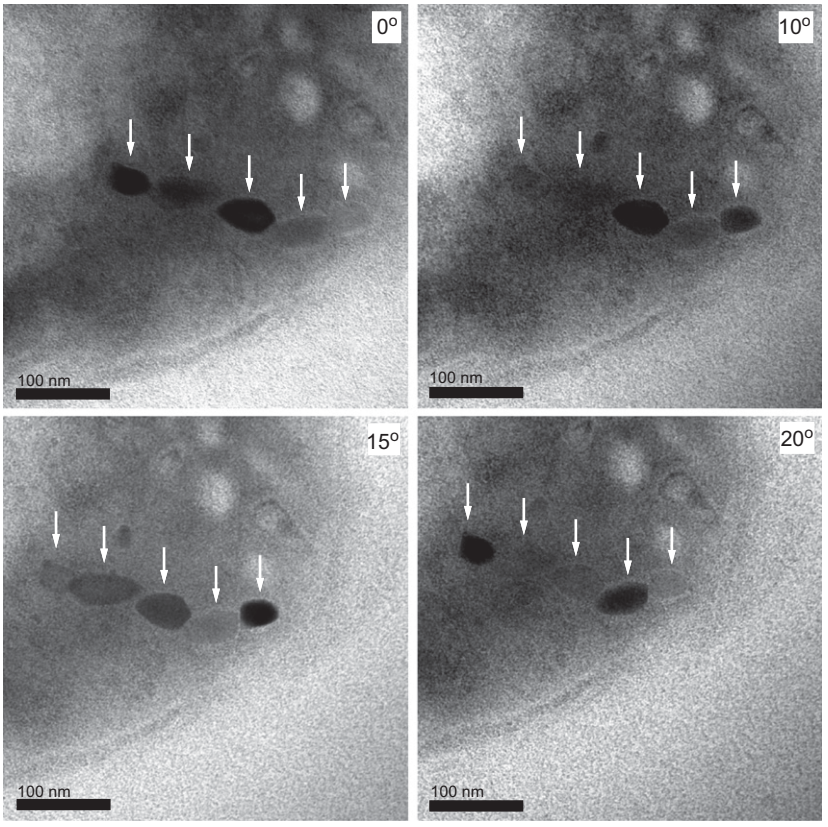

Fig. S5. Individual magnetite crystals in the magnetosome chain appear more or less electron-dense, depending on their angle with respect to the electron beam of a transmission electron microscope. The images are transmission electron micrographs of a cryo-ultrathin section of RS-1 tilted at 10°, 15°, and 20° from the original position (0°). The arrows highlight the five crystals in the chain.

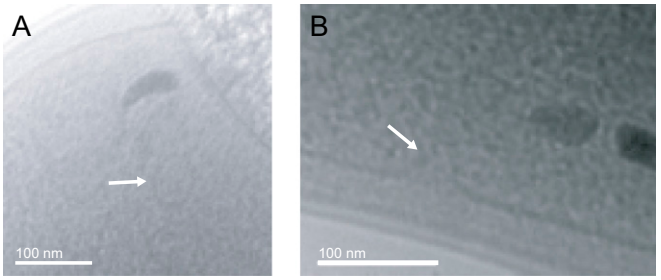

Fig. S6. Cryo-electron microscopy images and cryo-tomography data of whole, unlysed RS-1 cells do not allow clear visualization of intracellular structures because of the thickness of the cells (>800 nm). Nevertheless, at the tips and internal edges of the intact cells, where the cell diameter is smallest, cytoplasmic vesicles (white arrow) (*A*) and invaginations of the inner membrane (white arrow) (*B*) are visible.

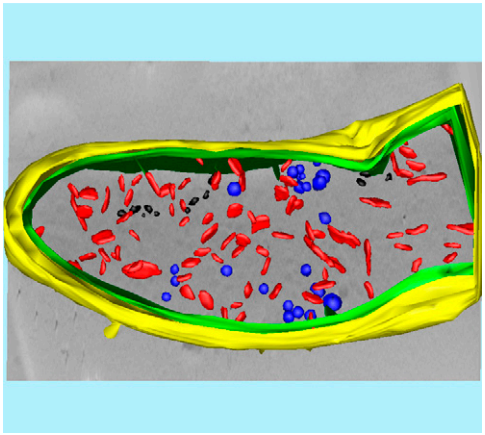

Movie S1. Cryo-electron tomography analysis and color modeling of a lysed RS-1 cell grown for 56 h in medium containing iron reveal extensive intracellular compartments near the periphery of the cell. Magnetite crystals are shown in black. The outer and inner membranes are shown in yellow and green, respectively. Round intracellular vesicles are shown in blue and the narrow, elongated compartments are shown in red.

Movie S1